Field survey of the 2017 Typhoon Hato and a comparison with storm surge modeling in Macau

Linlin Li[1*], Jie Yang[2,3*], Chuan-Yao Lin[4], Constance Ting Chua[5], Yu Wang[1,6], Kuifeng Zhao[2], Yun-Ta Wu[2,7], Philip Li-Fan Liu[2,8,9], Adam D. Switzer[1,5], Kai Meng Mok[10], Peitao Wang[11], Dongju Peng[1]

[1]Earth Observatory of Singapore, Nanyang Technological University, Singapore

[2]Department of Civil and Environmental Engineering, National University of Singapore, Singapore

[3]College of Harbor, Coastal and Offshore Engineering, Hohai University, China

[4]Research Center for Environmental Changes, Academia Sinica, Taipei 115, Taiwan

[5]Asian School of the Environment, Nanyang Technological University, Singapore

[6]Department of Geosciences, National Taiwan University, Taipei, Taiwan

[7]Department of Water Resources and Environmental Engineering, Tamkang University, New Taipei City, Taiwan

[8]School of Civil and Environmental Engineering, Cornell University, USA

[9]Institute of Hydrological and Ocean Research, National Central University, Taiwan

[10]Department of Civil and Environmental Engineering, University of Macau, Macau, China

[11]National Marine Environmental Forecasting Center, Beijing, China

Corresponding to: Linlin Li (llli@ntu.edu.sg) ; Jie Yang (jie_yang@hhu.edu.cn)

Abstract: On August 23, 2017 a Category 3 Typhoon Hato struck Southern China. Among the hardest hit cities, Macau experienced the worst flooding since 1925. In this paper, we present a high-resolution survey map recording inundation depths and distances at 278 sites in Macau. We show that one half of the Macau Peninsula was inundated with the extent largely confined by the hilly topography. The Inner Harbor area suffered the most with the maximum inundation depth of 3.1m at the coast. Using a combination of numerical models, we simulate and reproduce this typhoon and storm surge event. We further investigate the effects of tidal level and sea level rise on coastal inundations in Macau during the landfall of a 'Hato like' event.

1 Introduction

On August 23, 2017, at approximately 12:50 pm local time Typhoon Hato made landfall near Zhuhai, which is located on the Southern coast of Guangdong province, China (Figure 1). With an estimated 1-minute sustained wind

28 speed of 185 km/h near its center and a minimum central pressure of 945 hPa, Typhoon Hato was a Category 3
29 Hurricane on the Saffir-Simpson scale. Typhoon Hato was one of the strongest typhoons to affect the coastal areas
30 of the Pearl River Estuary (PRE) in Southern China over the last several decades. It caused widespread coastal
31 flooding in the PRE areas (ESCAP/WMO Typhoon Committee, 2017). Major cities in the northeast quadrant of the
32 typhoon track, including Macau, Zhuhai and Hong Kong, were severely affected. The resulting maximum storm
33 surge heights (water level above the astronomical tide) reached 1.62 m at A-Ma station in Macau, the highest since
34 water level recording began in 1925. Elsewhere in the PRE areas, a maximum storm surge of 2.79 m was recorded at
35 Zhuhai, and 1.18m, 1.65m and 2.42 m at Quarry Bay, Tai Po Kau and Tsim Bei Tsui in Hong Kong, respectively
36 (HKO, 2017) (Figure 1b). The extreme flooding in Macau was historically unprecedented in terms of the inundation
37 depth as well as the extent, and more than half of the Macau Peninsula was inundated. Typhoon Hato's strong wind
38 and the associated flooding resulted in 22 fatalities and caused 3.5 billion USD direct economic losses (Benfield,
39 2018).

40 Macau (and Hong Kong) commonly experience about 5-6 typhoons per year (Lee et al., 2012) and as the result the
41 low-lying area in the western part of Macau Peninsula has been frequently flooded by storm surges during major
42 typhoons. Relatively recent typhoons such as Becky (1993), Hagupit (2008), Koppu (2009), and Vicente (2012) all
43 generated storm surges that produced maximum inundation depths > 1 m in Macau, while the unnamed historical
44 typhoons in 1927 and 1948, and typhoon Gloria (1957) generated storm surges > 1.15 m (see the historical flood
45 records http://www.smg.gov.mo/smg/database/e_stormsurge_historicalRec.htm). Although frequently affected by
46 storm surges, the extreme inundation brought by Typhoon Hato still caught Macau unprepared. Consequently, the
47 local government has declared Typhoon Hato as the "worst-case" scenario and will use it as a criterion for designing
48 new engineering measures for coastal protection.

49 While Typhoon Hato has caused the worst flood event in Macau's history, the key flood parameters (e.g. the water
50 depth and inundation distance) have not been properly documented. Although, Macau has 2 tidal gauge stations and
51 17   inland   water   gauge   stations   distributed   in   the   areas   susceptible   to   flooding
52 (http://www.smg.gov.mo/smg/ftgms/e_ftgms.htm). Unfortunately, they all failed to record the peak water level due
53 to breakdown or electricity interruption of devices during Hato (SMG, 2017). Therefore, post event surveys of key
54 flood parameters become essential for better understanding storm surge dynamics and inundation characteristics
55 (e.g. Fritz et al., 2007;Tajima et al., 2014;Takagi et al., 2017;Soria et al., 2016). For this reason, our field survey
56 team was deployed to Macau and Zhuhai on August 26, 2017 and collected flood and damage information for 5
57 days. Here, the survey data have been analyzed and used to produce a high-resolution inundation map of Macau.

58 Qualitatively speaking, several factors have contributed to the exceptional damage during Typhoon Hato: 1)
59 Typhoon Hato occurred during the second day of a Lunar month and the landfall time roughly coincided with the
60 astronomical high tide; 2) According to the record, Typhoon Hato's wind speed was the strongest among all the
61 typhoons in Macau since 1953. The peak wind gust reached 217.4 km/h in Taipa Grande station and broke the
62 record of 211.0 km/h set by Typhoon Ruby in 1964 (SMG, 2017;Shan et al., 2018). 3) The translation wind speed of
63 Typhoon Hato exceeded 30 km/h (Takagi et al., 2018) before its landfall, which is unusually high compared with the

64   average transitional speed of 10-15 km/h in the South China Sea (Shan et al., 2018). 4) According to Hong Kong

65   Observatory, Typhoon Hato momentarily became a super typhoon during its approach towards the Pearl River

66   Estuary in the morning of August 23 (HKO, 2017). The sudden intensification occurred because of the low vertical

67   wind shear and the high sea surface temperature of ~31°C in the Northern portion of the SCS (HKO, 2017).

68   It is well-known that the tide during a typhoon's landfall plays a significant role in the severity of the storm surge

69   induced inundation. In the case of Typhoon Hato, the coincidence of astronomical high tide and the landfall time is

70   thought to be the major factor causing the wide-spread flooding in Macau. However, using the OSU TPXO-atlas8

71   tide model (Egbert and Erofeeva, 2002) and the tide gauge location (113.551 ° E 22.167 ° N) in Macau, we

72   estimated the peak tidal level on the day of Hato's landfall occurred at 10:00 AM on August 23, 2017 with the tide

73   level of 0.927 m above the mean sea level (MSL), while the estimated tidal level was only 0.470 m above the MSL

74   at the reported Typhoon Hato's landfall time around 12:50 pm on August 23, 2017. Thus, Typhoon Hato actually

75   made landfall almost 3 hours after the peak tidal level, while the tidal level differences are almost 0.5 meter. Thus,

76   it is intriguing to ask what if Typhoon Hato had occurred at a different time with a lower or higher tidal level, how

77   would the inundation areas change?

78   To provide a quantitative answer for the question posted above, a numerical simulation tool must be validated first.

79   In this paper, the tide-surge-wave coupled hydrodynamic model, SCHISM (Semi-implicit Cross-scale Hydroscience

80   Integrated System Model) (Zhang et al., 2016) is combined with the Weather Research and Forecasting (WRF)

81   model (Skamarock et al., 2008) to simulate the entire Typhoon Hato event. The high-resolution bathymetric data in

82   PRE and topographic data in Macau are employed for calculating coastal flooding. Model-data comparisons are

83   performed to ensure that the wind fields are reproduced well by the WRF model. The field survey data (e.g.

84   inundation depth and area) are used to check the accuracy of the storm surge model. Once the numerical model is

85   validated, we can use it to conduct a series of numerical experiments to assess the possible impact of 'Hato-like'

86   typhoon occurring at different tidal levels. Then looking at such hazard event and its counter-measures from a long-

87   term perspective, we examined the effect of sea level rise (SLR) on the inundation areas.

88   The paper is presented in the following order. We first report a high-resolution inundation map of Macau based on

89   our field measurements and observations. Then we describe each component of the numerical simulation package

90   followed by the simulation results of Typhoon Hato. Finally, we discuss the effect of tidal level and SLR through the

91   results of numerical experiments.

92   **2 Post-typhoon field survey**

93   On August 26, 2017, three days after Typhoon Hato made landfall, our survey team arrived at Macau, where they

94   surveyed ~ 300 sites in Macau Peninsula, measuring flow depths (water depth above the street level), maximum

95   runup, and inundation distances (Table S1). The team also recorded building damage. The team was able to conduct

96   interviews with many shopkeepers, homeowners and security officers, who witnessed this flood event. The

97   maximum inundation depths were mainly determined by using watermarks as indicators and where possible

98   confirmed by eyewitnesses. Watermarks identified on glass panels, iron gates and light colored walls were

99   photographed (Figure 2) and located using GPS. Inundation extent was determined by tracing watermarks from the

100 coastline to the inundation limit along streets perpendicular to the coastline. Distances between two surveyed sites

101 were about 20 - 25 m apart to ensure the high resolution of this survey map. In total, 278 inundation depths were

102 recorded and eyewitnesses confirmed 96 (35%) of them (Table S1).

103 Figure 3a shows the surveyed inundation depths on the Macau Peninsula. Names of the locations are marked on a

104 high-resolution bare ground elevation map in Figure 3b. The Inner Harbor area, which starts from the A-Ma Temple

105 in the southwest and ends at Qingzhou in the northwest of Macau Peninsula, was completely flooded to a depth of

106 3.1 m at Ponte Pou Heng (the purple dot in Fig 3a). Along the coastal roads of the Inner Harbor, inundation depth

107 reached 2.0 - 2.5m in many low-lying places. When tracing the watermarks along the two major streets: Avenida de

108 Almeida Ribeiro and Ruo Do Gamboa, we observe that, as the seawater penetrated inland, the inundation depth

109 gradually decreased from > 2 m to ~1 m (Fig 3c-d). The inundation extent was clearly confined by the hilly

110 topography (Figure 3a-b). From south to north, the steep topography of the local hills acted as natural barriers,

111 limiting flood propagation. In contrast, the relatively flat (2-3 m above mean sea level) northwest area surrounding

112 "Fai Chi Kei", experienced inundation distances of up to ~1.3 km inland (Figure 3a-b). The coastal area in the

113 northeast was largely spared due to the seawall protection and slightly higher elevation, while the southeast coastal

114 area was slightly flooded by less than 1 m surge with limited inundation distance (<50 m). Considering the size of

115 the Macau Peninsula, which is ~3 km E-W and ~4 km N-S, nearly half of the peninsula was inundated during

116 Typhoon Hato (Figure 3a).

117 Notably, many eyewitnesses commented that this flooding event was characterized by rapid-rising speed;

118 shopkeepers in the Inner Harbor area stated that seawater rose quickly from the ankle level to chest high in less than

119 20 minutes, leaving them no time to rescue property or possessions on the ground floor. The ground-floors of most

120 of buildings in Macau are used for commercial purpose, which partly explains why Macau had suffered from

121 economic loss exceeding 1.42 billion USD (HKO, 2017). Although residents who live in the Inner Harbor area are

122 experienced in battling chronic flooding caused by storm surges, the extreme flood caused by Typhoon Hato still

123 came as a surprise for them in many ways (e.g. its speed, depth and extent). In one of the interviews, an elderly

124 resident who lives on the street of Rua Do Camboa used the length of his body as a yardstick to describe the height

125 of floodwater from previous events. He explained that Typhoon Becky (1993) had resulted in approximately 1.4

126 m floodwater at where he lives; 1.2 m during Typhoon Hagupit (2008); 0.3 m during Typhoon Vicente (2012); and

127 this time Typhoon Hato had resulted in a 2.1 m flood height.

128 The survey data presented in this study is complementary to the data provided by an earlier study (Takagi et al.,

129 2018) in terms of the number of surveyed locations and spatial coverage. Takagi et al. (2018) provided 12 data

130 points in Macau and Hong Kong while our 278 data points are concentrated in Macau with the purpose of

131 constructing a measured high-resolution inundation map. Such map provides not only valuable documentation of

132 such rare and extreme event but also validation data for numerical modelers.

133   **3 Numerical simulation**

134   The WRF model (version 3.8.1) (Skamarock et al., 2008) is used to generate the wind and pressure fields of

135   Typhoon Hato. The initial and meteorological boundary conditions for WRF were obtained from the National

136   Center for Environmental Prediction (NCEP) Global Forecast System (GFS) with $0.5° \times 0.5°$ analysis data sets at 6-

137   h interval. The time-varying sea surface temperature (SST) was obtained from $0.5°$ NCEP real-time-global data set.

138   The planetary boundary layer of the Yonsei University boundary layer scheme (Hong et al., 2006) was used with the

139   revised MM5 similarity surface layer scheme (Jiménez et al., 2012) and the unified Noah land surface model

140   (Tewari et al., 2004) over land. The single-moment five-class microphysics scheme (Hong et al., 2004), the updated

141   Kain-Fritsch scheme (Kain, 2004) with a moisture-advection based trigger function (Ma and Tan, 2009), the Rapid

142   Radiation Transfer Model for Global Circulation Models (RRTMG) shortwave and longwave schemes (Iacono et

143   al., 2008) are also adopted in this study. The horizontal resolution of the model is 3 km and the grid box had 921 $\times$

144   593 points in both east-west and north-south directions. There were 45 vertical levels with the lowest level

145   approximately 50 m above the surface. The output time interval of wind and pressure fields is 10 minutes.

146   The output wind and pressure fields from the WRF results are then used to drive the storm surge simulation in the

147   tide-surge-wave coupled hydrodynamic model SCHISM (Zhang et al., 2016), which is a derivative code of the

148   original SELFE (Semi-implicit Eulerian-Lagrangian Finite Element) model. The SCHISM system has been

149   extensively tested against Standard Ocean/coastal benchmarks and applied to several regional estuaries for storm-

150   surge inundation modeling (Krien et al., 2017;Wang et al., 2014). In this study, the model is used in the 2DH

151   barotropic mode, which solves nonlinear shallow water equations on unstructured meshes for storm surges. To track

152   the coastline movements, the model includes an efficient wetting-drying algorithm by using semi-implicit time

153   stepping and Eulerian-Lagrangian method for advection (Zhang and Baptista, 2008).

154   The bottom shear stress is modeled by the Manning's formula with the Manning coefficient being set to 0.025 for

155   the inland area (area above mean sea level) and 0.01 for the offshore area. The values of Manning coefficient are

156   informed by previous studies (e.g. Martyr et al., 2013;Garzon and Ferreira, 2016). We choose relatively low

157   Manning value for the estuary and open sea area as the sediment in the Pearl River Estuary is dominated by very

158   fine sand (mainly silt clays) (Jiang et al., 2014). The drag coefficient for the surface wind stress is computed

159   according to Pond and Pickard (1998). The model is forced by applying tidal elevation series on nodes along open

160   ocean boundaries, which are extracted from the OSU TOPEX/Poseidon Global Inverse Solution model TPXO8-atlas

161   (Egbert and Erofeeva, 2002).

162   To capture the effects of wind waves in the storm surge simulation, the spectral Wind Wave Model (WWMIII) is

163   employed. WWMIII solves the wave action equations in the frequency domain on the same unstructured grid as

164   SCHISM. Physical processes including wave growth and energy dissipation due to whitecapping, nonlinear

165   interaction in deep and shallow waters, and wave breaking are all considered in the simulations. The WWMIII is

166   dynamically coupled with SCHISM every 600 seconds. The radiation stress is estimated according to (Roland,

167   2008) based on the directional spectra itself. The radiation stresses computed in WWMIII are transferred to
168   SCHISM at each step to update water level and velocity, which are sent as feedback reversely.

169

170   For Typhoon Hato, the simulation domain covers the northern part of the South China Sea (Figure 4a). We create an
171   unstructured grid with horizontal resolution varying from 50 km in the deep sea, ~ 1 km over the shelf to ~ 20 m in
172   the vicinity of Macau (Figure 4b-c). To ensure the accuracy and reliability of the simulation results, we integrated as
173   many available topographic and bathymetric data as possible: 1) The bathymetric data in the Pearl River Estuary are
174   integrated from 36 nautical charts with scales ranging from 1:5000 to 1:250000; 2) high resolution topographic data
175   for Macau is purchased from the Macau Cartography and Cadastre Bureau; 3) 1-arc Shuttle Radar Topography
176   Mission (SRTM) data covering the Pearl River Delta; (c) 5m elevation is specified for the two artificial islands in
177   the eastern side of Macau Peninsula, which are still under construction. The topographic and bathymetric data were
178   complemented by 30 arc seconds General Bathymetric Chart of the Oceans (GEBCO) data and integrated into one
179   dataset after being adjusted to the mean sea level (MSL). Using this model setting, we validated the tidal current
180   model performs well when comparing the simulated tidal cycle with measured data from 1 Nov 2014 to 30 Nov
181   2014 (Figure S1).

182   **4 Results**

183   **4.1 Simulation results of Typhoon Hato**

184   We first compare the wind speeds generated by WRF with the measured data at 9 selected wind gauge stations in the
185   PRE (Figure 5c-k), including 4 local wind gauges in Macau (see the gauge locations in Figure 5a-b). The model/data
186   comparison shows that the WRF model captures Typhoon Hato's wind fields well in terms of both the peak wind
187   speed and the phase (Figure 5c-k).

188   The simulated maximum surge heights in the PRE (Figure 6a) show that the storm surge heights on both sides of the
189   PRE varied widely, ranging from 0 m to 4.5 m. Surge heights > 2.5 m occurred on much of the western side of PRE
190   including Macau. Wave amplification effects, the funnel-shaped coastline in the PRE also likely led to larger surge
191   heights in the inner estuary area. To validate the numerical results, we compare the simulated storm-tides with the
192   measured storm-tides at 4 selected locations (Figure 6b). Very reasonable agreements are observed, ensuring the
193   reliability of the modeling approach used in this study.

194   We further compare the simulated and measured inundation maps in Macau (Figure 6c). The calculated inundation
195   depths are slightly lower (~10%) than the measured ones in some locations near the coastline of "Fai Chi Kei" and
196   southern Inner Harbor and several inland locations in Inner Harbor (see the locations in Figure 3b). The
197   underestimation is likely the by-product of the bare-ground topographic data used in the simulation, which does not
198   include buildings, and hence excludes complex flow patterns (e.g. wave front colliding with buildings) and
199   channeling effects, which locally increase water depth. Nevertheless, the overall agreement is quite good. It

200　demonstrates that the coupled model can reproduce this flood event reasonably well in terms of both inundation
201　depth and extent.

202　In Figure 6d we also plot the simulated arrival time of wave front, which can be viewed as the arrival time of the
203　surge. During Typhoon Hato the surge wave arrived in the southern Inner Harbor first at the local time around
204　11:20 on August 23, 2017 and then propagated eastward inland and northward in the Fai Chi Kei direction in the
205　next one and half hours. The flow velocity was less than 0.5 m/s in the southern Inner Harbor due to the generally
206　steep slope, while in the area surrounding Fai Chi Kei, the flow velocity was faster and was up to 0.7 - 0.8 m/s.
207　When comparing with the 2 – 5 m/s tsunami flow velocity recorded in the Banda Aceh during the 2004 Indian
208　Ocean tsunami (Fritz et al., 2006), the 0.5-0.8 m/s flow velocity of storm tide in Macau is significantly smaller. The
209　information like this demonstrates that numerical model and field survey can complement each other and recover a
210　comprehensive view of disaster scene.

211　**4.2 The effects of tidal level**

212　Having checked our numerical model with measured data and demonstrated that the model can replicate events like
213　Typhoon Hato, we now investigate the effects of tidal level on coastal flooding. Most the PRE including Macau has
214　a mixed semidiurnal tidal cycle in which the semidiurnal lunar tide, M2, is the predominant component followed by
215　K1, O1 and S2. The maximum tidal range observed in Macau is 2.86 m while the difference between mean high
216　water (MHW) and mean low water (MLW) is 1.11 m (calculated from the tide record during 1985-2012).

217　To quantitatively investigate the impact of tidal level at Hato's landfall, we first selected two extreme tidal levels
218　from the years of 1964-2017 using OSU TPXO-atlas8 tide model. The reason we use more extreme tidal levels is
219　because scenarios under those tidal levels can provide the upper and lower bounds of the potential inundations, thus
220　better demonstrating the effect of tidal level. On the other hand, we observe the peak tidal level on the day of
221　Typhoon Hato's landfall was only moderately high compared with the daily higher high water records (HHW) in
222　Macau (Figure S2) although it was the third highest during that month. Putting this peak tide of 0.927 m in all the
223　estimated daily HHW, we can see that this value is lower than 21% of the daily HHW during 1964-2017 (Figure S2
224　shows the HHW and LLW during 2008-2017 as an example). We find the corresponding highest extreme tide
225　(HET) and the lowest extreme tide (LET) occurred on January 1st , 1987 at 22:00 and January 2nd , 1987 at 6:00,
226　respectively with the tide 1.304 m above MSL and 1.165 m below MSL. We then conduct storm surge simulations
227　at these two selected extreme tidal levels by moving the typhoon landfall time from 13:00 (UTC+8), Aug 23, 2017
228　to January 1st, 1987 at 22:00 and January 2nd , 1987 at 6:00 local time.

229　Figure 7 shows the maximum inundation maps for the real case (benchmark scenario, Figure 7a), at HET (Figure
230　7b) and LET (Figure 7c), respectively. The striking observation is that Typhoon Hato would cause inundation in
231　Macau at all the considered tidal levels (Figure 7a-c). Even Typhoon Hato occurred during the LET, the Inner
232　Harbor area would still be inundated with the maximum inundation depth up to 1.0 m (Figure 7c). We emphasize
233　here, as the LET is a representative value of the lowest extreme tidal level in the past 54 years (1964-2017), which

7

234   suggests the Inner Harbor area will certainly be inundated during Hato-like events regardless of the tidal levels at the
235   landfall time. The results once again highlighted the vulnerability of the Inner Harbor area to extreme flooding and
236   urgency of establishing effective protection system. Not surprisingly, if Hato had occurred at HET, a noticeably
237   greater inundation depth (0.5-0.8 m deeper in the Inner Harbor, see Figure 8) would have been sustained in all the
238   flooded areas on the Macau Peninsula with inundation extending considerably to previously unaffected areas. For
239   example, had Hato struck at the HET, the northeast Macau Peninsula, the coastal area of Taipa and Cotai would be
240   inundated with up to 1-m water depth or higher.

241   **4.3 Investigation sea level rise**

242   To account for the effects of future sea level rise (SLR), the values of 0.5 m and 1 m SLR were chosen to represent
243   the sea levels by the mid-century and end of this century based on projected local sea level rises of 30-51 cm by
244   2060 and 65-118 cm by 2100 (Wang et al., 2016). We then ran the storm surge simulations at HET and LET with
245   different magnitude of SLR 0.5 m and 1.0 m. For each simulation, we obtain the maximum inundation depths at all
246   in-land computational nodes by subtracting the DEM data from the simulated maximum wave heights. In total, we
247   derive three sets of inundation maps at current sea level, 0.5 m and 1.0 m SLR condition.

248   Adding the effect of 0.5-m and 1-m SLR at HET, the inundation extent quickly expands into the eastern part of the
249   Macau Peninsula and coastal areas of Taipa, Cotai and University of Macau, where no or limited flood was observed
250   during Typhoon Hato (Figure 9a-b). Compared with the benchmark scenario (Figure 7a), the maximum inundation
251   depths in inner harbour area will increase more than 1-1.2 m in the 0.5-m SLR scenario (Figure 9e) and 1.2-1.5 m in
252   the 1-m SLR scenario for most of the inner harbour area (Figure 9i); such increase is generally a linear combination
253   of increased tidal level and SLR. While in the eastern side of Macau Peninsula and some places in Taipa and Cotai,
254   we observe larger increases in the water depths than in the inner harbour area. The increased water depths can be up
255   to 1.2-1.5 m and 1.5-2.0 m at 0.5-m and 1-m SLR conditions, respectively. The larger increase can be partly
256   attributed to large waves in the eastern side of Macau Peninsula, coastal areas of Taipa and Cotai than in the inner
257   harbour area, especially at higher sea level conditions (Figure 10). Such spatially non-uniform response of storm
258   waves to SLR has been discussed in previous studies in many coastal areas worldwide (e.g. Atkinson et al.,
259   2013;Bilskie et al., 2016;Mcinnes et al., 2003) and China (e.g. Wang et al., 2012;Yin et al., 2017). Comparing the
260   maximum inundation depth between scenarios at LET under different sea level conditions (Figure 9c-d), we point
261   out once again that the Inner Harbor area will suffer increasingly more hazardous inundation with the rising sea
262   level. Thus engineer measures are urgently required to protect this area. When designing such engineer measures,
263   proactive policies and adaptive strategies should be taken to combat the likelihood of worsening flooding in future.

264   **5 Conclusions**

265   Typhoon Hato was one of the most damaging natural disaster events in the Western Pacific region in 2017. It caused
266   extensive coastal inundation in and around the Pearl River Delta region. In this paper, we have presented a detailed

267   post-typhoon field survey, yielding 278 measurements of maximum water depths and inundation extent on Macau

268   Peninsula. Using these data, a high-resolution flood map has been produced. These survey data have been used to

269   successfully validate a numerical model package, which consists of a WRF model for calculating the wind and

270   atmospheric pressure field and a tide-surge-wave coupled hydrodynamic model, SCHISM, for computing tides,

271   storm surges and ocean waves driven by the WRF model results. The data-model comparisons show that the skills of

272   the numerical model package are high and can capture all key features of this event, including the wind fields, the

273   water levels associated with storm surges and tides in the PRE, and the inundation depths in Macau. More

274   importantly, the numerical model package can provide additional information such as the arrival times of the storm

275   surge front and the corresponding shoreline movements.

276   The numerical model package can also be used to gain better understanding of the relative importance of different

277   causes for coastal flooding. To demonstrate this capability, we have focused on studying the effects of tidal level

278   and SLR on coastal inundation in Macau, using Typhoon Hato's atmospheric condition as a benchmark scenario.

279   One of the important observations is that regardless the tidal level during Typhoon Hato's landfall, the Inner Harbor

280   area will always be inundated with the maximum inundation depth up to 0.5 -1.0 m. On the other hand, although

281   Typhoon Hato broke all the historical records in terms of storm surge heights and flooded area, much worse scenario

282   could be expected if Typhoon Hato had occurred at a higher tidal level, and thus, caution is required if Typhoon

283   Hato is to be used as the worst-case scenario for designing future coastal defense measures. This is especially true

284   when taking the rising sea level into consideration as 0.5-m and 1-m SLR could significantly increase the severity of

285   the resulting inundation for most of the territory in Macau, including both the high tide and low tide conditions. The

286   inundation maps presented in this study provide the lower and upper bound of potential impacts of Hato-like events

287   at different tidal levels and sea level conditions. Such maps could aid the local government to make more

288   informative decisions.

289   Besides the tidal level, other factors including the landing location, track azimuth, forward speed, the sudden

290   intensification and urban development (e.g. land reclamation) may play more important role in contributing to this

291   record-breaking flood in Macau. The effects of such factors are being analyzed in more detail in a future paper.

292   Hato-like typhoon events pose a clear and significant threat to the emerging mega-cities area of the PRD and the

293   drive to expand towards the sea with extensive land reclamation and infrastructure development needed to meet the

294   demands of the growing population and the booming economy. Although most major cities in the region are

295   protected by seawalls, the protection standards vary considerably and whether such standards are sufficient to

296   combat increasingly frequent flooding in future needs careful investigation. Adaptive strategies and sustainable

297   management are almost certainly required in order to keep up with the pace of rising sea level. We believe that the

298   data and findings provided in this paper and the numerical model package will not only be of great interest to coastal

299   hazard researchers, but also to a range of stakeholders such as policy makers, town planners, emergency services

300   and insurance companies who are working to create or insure safer coastlines.

References

Atkinson, J., McKee Smith, J., and Bender, C.: Sea-Level Rise Effects on Storm Surge and Nearshore Waves on the Texas Coast: Influence of Landscape and Storm Characteristics, Journal of Waterway, Port, Coastal, and Ocean Engineering, 139, 98-117, 10.1061/(ASCE)WW.1943-5460.0000187, 2013.

Benfield, A.: Weather, Climate & Catastrophe Insight 2017 Annual Report, Aon Benfield, https://reliefweb.int/sites/reliefweb.int/files/resources/20180124-ab-if-annual-report-weather-climate-2017.pdf, 2018.

Bilskie, M. V., Hagen, S. C., Alizad, K., Medeiros, S. C., Passeri, D. L., Needham, H. F., and Cox, A.: Dynamic simulation and numerical analysis of hurricane storm surge under sea level rise with geomorphologic changes along the northern Gulf of Mexico, Earth's Future, 4, 177-193, doi:10.1002/2015EF000347, 2016.

Egbert, G. D., and Erofeeva, S. Y.: Efficient Inverse Modeling of Barotropic Ocean Tides, Journal of Atmospheric and Oceanic Technology, 19, 183-204, 10.1175/1520-0426(2002)019<0183:EIMOBO>2.0.CO;2, 2002.

ESCAP/WMO Typhoon Committee, C.: Member Report, http://www.typhooncommittee.org/12IWS/docs/Members/China20171026_final.pdf, 2017.

Fritz, H., C., B. J., E., S. C., and Jeseon, Y.: 2004 Indian Ocean tsunami flow velocity measurements from survivor videos, Geophysical Research Letters, 33, doi:10.1029/2006GL026784, 2006.

Fritz, H. M., Blount, C., Sokoloski, R., Singleton, J., Fuggle, A., McAdoo, B. G., Moore, A., Grass, C., and Tate, B.: Hurricane Katrina storm surge distribution and field observations on the Mississippi Barrier Islands, Estuarine, Coastal and Shelf Science, 74, 12-20, https://doi.org/10.1016/j.ecss.2007.03.015, 2007.

Garzon, J., and Ferreira, C.: Storm Surge Modeling in Large Estuaries: Sensitivity Analyses to Parameters and Physical Processes in the Chesapeake Bay, Journal of Marine Science and Engineering, 4, 45, 2016.

HKO: Super Typhoon Hato (1713), Hong Kong Observatory, http://www.weather.gov.hk/informtc/hato17/report.htm, 2017.

Hong, S.-Y., Dudhia, J., and Chen, S.-H.: A Revised Approach to Ice Microphysical Processes for the Bulk Parameterization of Clouds and Precipitation, Monthly Weather Review, 132, 103-120, 10.1175/1520-0493(2004)132<0103:ARATIM>2.0.CO;2, 2004.

Hong, S.-Y., Noh, Y., and Dudhia, J.: A New Vertical Diffusion Package with an Explicit Treatment of Entrainment Processes, Monthly Weather Review, 134, 2318-2341, 10.1175/mwr3199.1, 2006.

344 Iacono, M. J., Delamere, J. S., Mlawer, E. J., Shephard, M. W., Clough, S. A., and Collins, W. D.: Radiative forcing
345 by long-lived greenhouse gases: Calculations with the AER radiative transfer models, Journal of Geophysical
346 Research: Atmospheres, 113, doi:10.1029/2008JD009944, 2008.
347 Jiang, S., Xu, F., Li, Y., Liu, X., Zhao, Y., and Xu, W.: Distributional characteristics of grain sizes of surface
348 sediments in the Zhujiang River Estuary, 30-36 pp., 2014.
349 Jiménez, P. A., Dudhia, J., González-Rouco, J. F., Navarro, J., Montávez, J. P., and García-Bustamante, E.: A
350 Revised Scheme for the WRF Surface Layer Formulation, Monthly Weather Review, 140, 898-918, 10.1175/mwr-d-
351 11-00056.1, 2012.
352 Kain, J. S.: The Kain–Fritsch Convective Parameterization: An Update, Journal of Applied Meteorology, 43, 170-
353 181, 10.1175/1520-0450(2004)043<0170:TKCPAU>2.0.CO;2, 2004.
354 Krien, Y., Testut, L., Islam, A. K. M. S., Bertin, X., Durand, F., Mayet, C., Tazkia, A. R., Becker, M., Calmant, S.,
355 Papa, F., Ballu, V., Shum, C. K., and Khan, Z. H.: Towards improved storm surge models in the northern Bay of
356 Bengal, Continental Shelf Research, 135, 58-73, https://doi.org/10.1016/j.csr.2017.01.014, 2017.
357 Lee, E. K. S., Fok, L., and Lee, H. F.: An Evaluation of Hong Kong's Tropical Cyclone Warning System, Asian
358 Geographer, 29, 131-144, 10.1080/10225706.2012.742619, 2012.
359 Ma, L.-M., and Tan, Z.-M.: Improving the behavior of the cumulus parameterization for tropical cyclone prediction:
360 Convection trigger, Atmospheric Research, 92, 190-211, https://doi.org/10.1016/j.atmosres.2008.09.022, 2009.
361 Martyr, R. C., Dietrich, J. C., Westerink, J. J., Kerr, P. C., Dawson, C., Smith, J. M., Pourtaheri, H., Powell, N.,
362 Ledden, M. V., Tanaka, S., Roberts, H. J., Westerink, H. J., and Westerink, L. G.: Simulating Hurricane Storm
363 Surge in the Lower Mississippi River under Varying Flow Conditions, Journal of Hydraulic Engineering, 139, 492-
364 501, doi:10.1061/(ASCE)HY.1943-7900.0000699, 2013.
365 Mcinnes, K. L., Walsh, K. J. E., Hubbert, G. D., and Beer, T.: Impact of Sea-level Rise and Storm Surges on a
366 Coastal Community, Natural Hazards, 30, 187-207, 10.1023/a:1026118417752, 2003.
367 Pond, S., and Pickard, G. L.: Introductory Dynamical Oceanography, Oxford : Elsevier Butterworth-Heinemann,
368 1998.
369 Roland, A.: Development of WWM II: Spectral wave modeling on unstructured meshes, 2008.
370 Shan, C., Zhang, X., Yuan, H., Qian, C., Huang, X., Jiang, X., Shen, H., Sun, S., Ji, Y., Li, J., Wang, C., Zhang, Y.,
371 Zhang, B., Zheng, J., Fu, M., and Qin, X.: The hazard assessment of Typhoon Hato in Macau, China National
372 Commission for Disaster Reduction, http://www.gep.gov.mo/event/pdf/reportCN_201803.pdf, 2018.
373 Skamarock, W. C., Klemp, J. B., Dudhia, J., Gill, D. O., Barker, D., Duda, M. G., Huang, X.-y., Wang, W., and
374 Powers, J. G.: A Description of the Advanced Research WRF Version 3, National Center for Atmospheric Research,
375 Boulder, Colorado, USA, NCAR TECHNICAL NOTE, 2008.
376 SMG: Typhoon Hato (1713), Macau Meteorological and Geophysical Bureau,
377 http://www.smg.gov.mo/smg/database/pdf/typhoon/e_1713.pdf, 2017.
378 Soria, J. L. A., Switzer, A. D., Villanoy, C. L., Fritz, H. M., Bilgera, P. H. T., Cabrera, O. C., Siringan, F. P., Maria,
379 Y. Y.-S., Ramos, R. D., and Fernandez, I. Q.: Repeat Storm Surge Disasters of Typhoon Haiyan and Its 1897
380 Predecessor in the Philippines, Bulletin of the American Meteorological Society, 97, 31-48, 10.1175/bams-d-14-
381 00245.1, 2016.
382 Tajima, Y., Yasuda, T., Pacheco, B. M., Cruz, E. C., Kawasaki, K., Nobuoka, H., Miyamoto, M., Asano, Y.,
383 Arikawa, T., Ortigas, N. M., Aquino, R., Mata, W., Valdez, J., and Briones, F.: Initial Report of JSCE-PICE Joint
384 Survey on the Storm Surge Disaster Caused by Typhoon Haiyan, Coastal Engineering Journal, 56, 1450006,
385 10.1142/s0578563414500065, 2014.
386 Takagi, H., Esteban, M., Shibayama, T., Mikami, T., Matsumaru, R., Leon, M. D., N.D.Thao, Oyama, T., and
387 Nakamura, R.: Track analysis, simulation, and field survey of the 2013 Typhoon Haiyan storm surge, Journal of
388 Flood Risk Management, 10, 42-52, doi:10.1111/jfr3.12136, 2017.
389 Takagi, H., Xiong, Y., and Furukawa, F.: Track analysis and storm surge investigation of 2017 Typhoon Hato: were
390 the warning signals issued in Macau and Hong Kong timed appropriately?, Georisk: Assessment and Management
391 of Risk for Engineered Systems and Geohazards, 1-11, 10.1080/17499518.2018.1465573, 2018.
392 Tewari, M., Chen, F., Wang, W., Dudhia, J., Lemone, M., Mitchell, K., Ek, M., Gayno, G., Wegiel, J., and Cuenca,
393 R.: Implementation and verification of the unified Noah land-surface model in the WRF model 20th Conference on
394 Weather Analysis and Forecasting/16th Conference on Numerical Weather Prediction, Seattle, WA, US, 2004.
395 Wang, H., Loftis, J., Liu, Z., Forrest, D., and Zhang, J.: The Storm Surge and Sub-Grid Inundation Modeling in New
396 York City during Hurricane Sandy, Journal of Marine Science and Engineering, 2, 226, 2014.
397 Wang, J., Gao, W., Xu, S., and Yu, L.: Evaluation of the combined risk of sea level rise, land subsidence, and storm
398 surges on the coastal areas of Shanghai, China, Climatic Change, 115, 537-558, 10.1007/s10584-012-0468-7, 2012.

11

399   Wang, L., Huang, G., Zhou, W., and Chen, W.: Historical change and future scenarios of sea level rise in Macau and
400   adjacent waters, Advances in Atmospheric Sciences, 33, 462-475, 10.1007/s00376-015-5047-1, 2016.
401   Yin, K., Xu, S., Huang, W., and Xie, Y.: Effects of sea level rise and typhoon intensity on storm surge and waves in
402   Pearl River Estuary, Ocean Engineering, 136, 80-93, https://doi.org/10.1016/j.oceaneng.2017.03.016, 2017.
403   Zhang, Y. J., and Baptista, A. M.: An Efficient and Robust Tsunami Model on Unstructured Grids. Part I:
404   Inundation Benchmarks, Pure and Applied Geophysics, 165, 2229-2248, 10.1007/s00024-008-0424-7, 2008.
405   Zhang, Y. J., Ye, F., Stanev, E. V., and Grashorn, S.: Seamless cross-scale modeling with SCHISM, Ocean
406   Modelling, 102, 64-81, https://doi.org/10.1016/j.ocemod.2016.05.002, 2016.

407

408

409
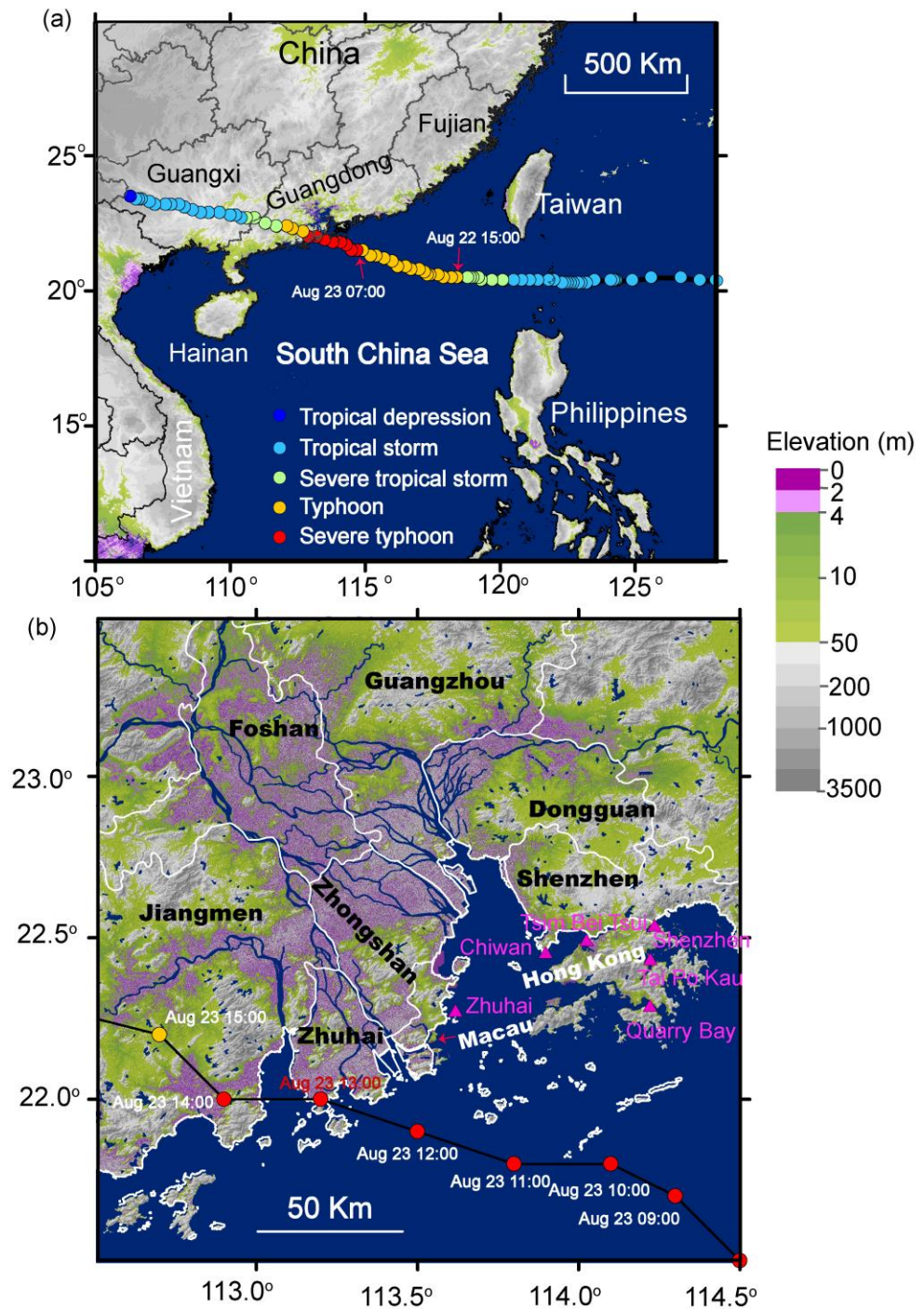
Figure 1. Typhoon Hato track data from the Chinese typhoon weather website (http://typhoon.weather.com.cn/). (a)
Typhoon Hato took a path extremely dangerous to the Pearl River Delta. It became a typhoon inside the South China
Sea at 15:00 on August 22, 2017 (local time) and further was intensified into a Severe Typhoon at 07:00 AM on
August 23 before making landfall at 12:50 PM in southern part of Zhuhai, China. (b) A close-up shows the landfall

13

414 location and the affected cities in the Pearl River Delta. Purple colors denote land elevation lower than 4 m above
415 mean sea level.

416

Longitude: 113.540481
Latitude: 22.202719

Longitude: 113.53676
Latitude: 22.199813

Longitude: 113.536548
Latitude: 22.198702

Longitude: 113.536638
Latitude: 22.19873

Longitude: 113.536192
Latitude: 22.194345

Longitude: 113.5339
Latitude: 22.18999

Longitude: 113.5368
Latitude: 22.196137

Longitude: 113.538539
Latitude: 22.194066

417

418 **Figure 2.** Photos taken during the field survey on the Macau Peninsula.

419
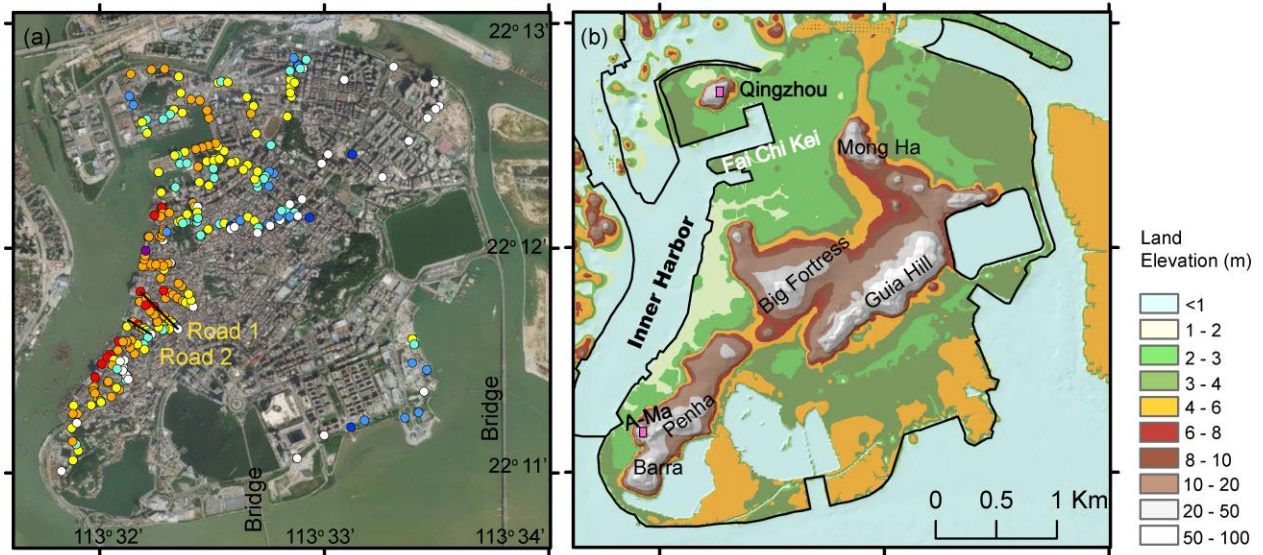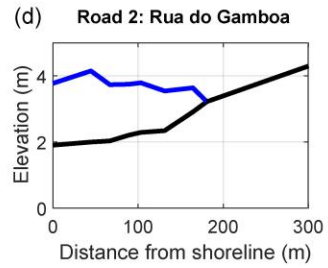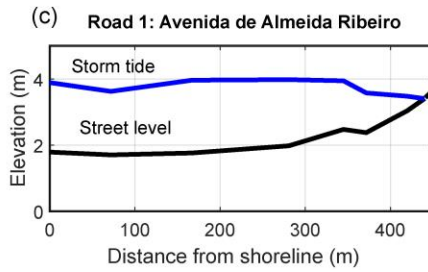
Figure 3. (a) Measured inundation depths on the Macau Peninsula shown on a Google Earth image. (b) High-resolution bare ground elevation with marked locations. (c) and (d) Profiles of surveyed inundation water depths along two main roads: Avenida de Almeida Ribeiro and Rua do Gamboa.
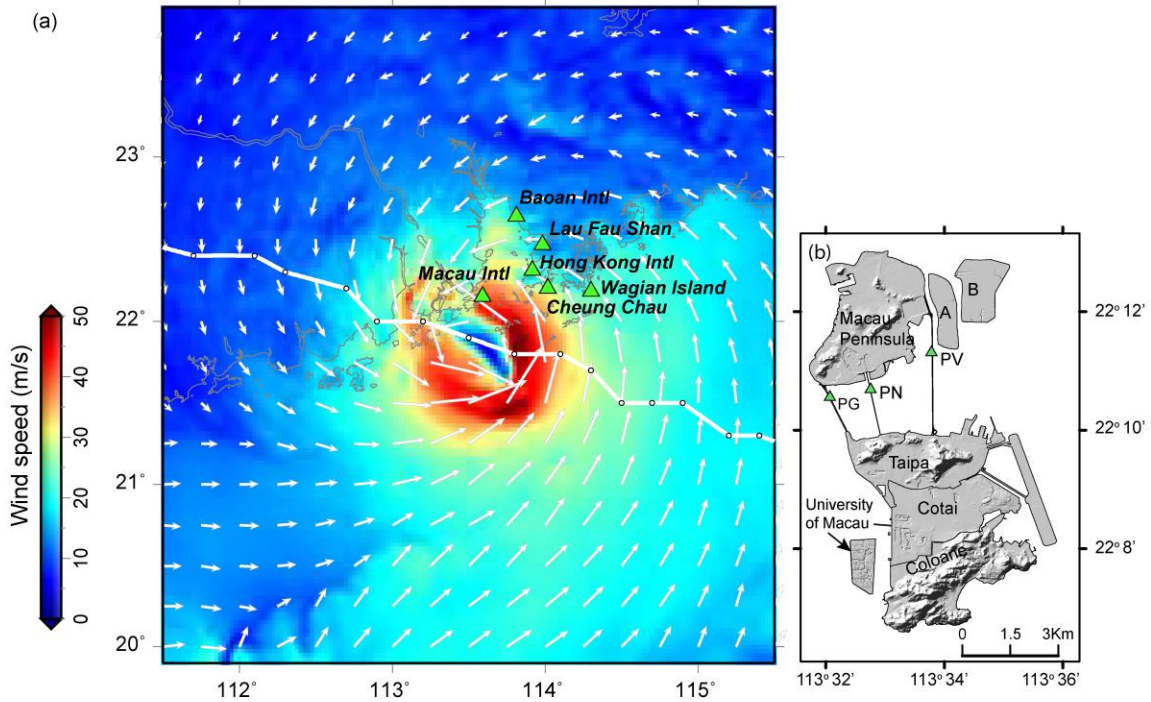
425
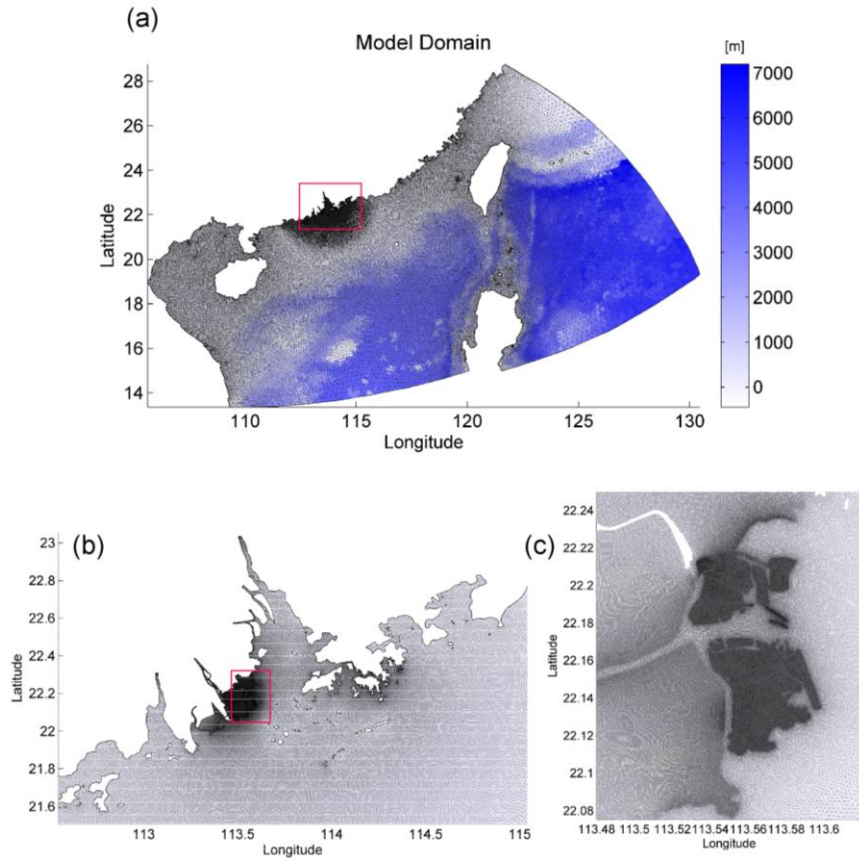
Figure 4. (a) The numerical simulation domain for SCHISM-WWMIII with close-ups showing (b) the mesh in PRD
and (c) the mesh near Macau.

428
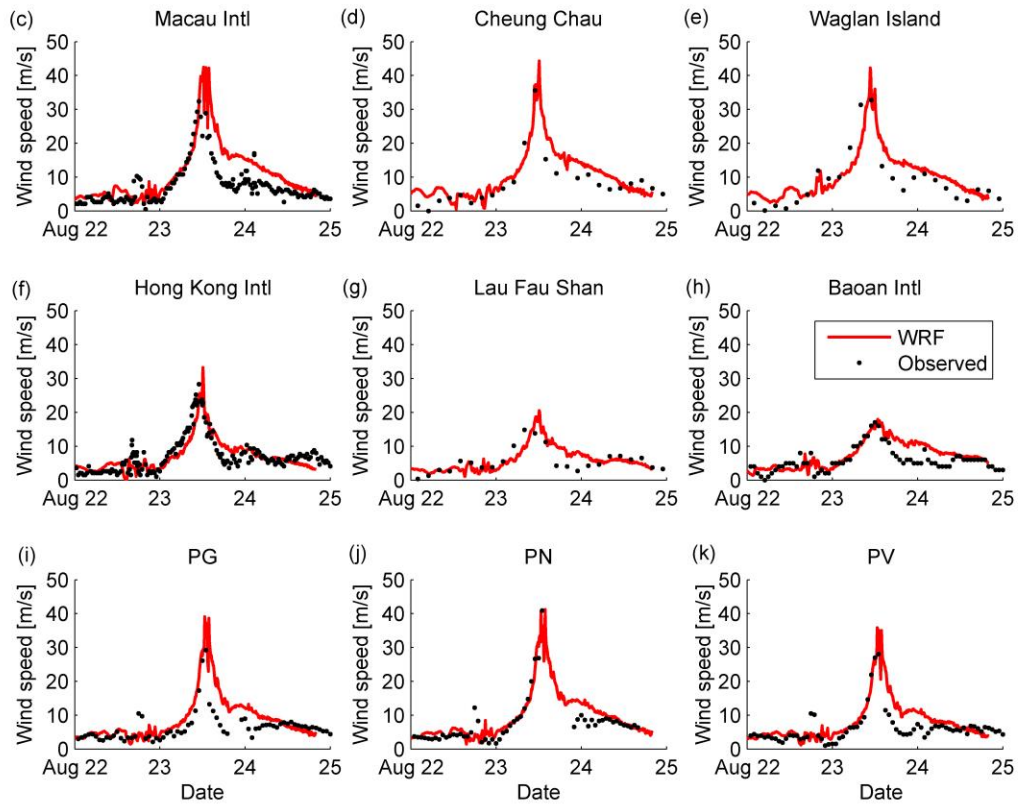
430 **Figure 5.** Wind fields generated by the WRF model: (a) In the Pearl River Estuary at 12:50 PM on August 23; (b)
431 The wind gauge locations of PG, PN and PV in Macau; (c) – (k) Comparisons of numerical results (WRF) with
432 measured wind speed at different locations. Locations and names of wind gauges (c) - (h) are shown in Figure 5a.
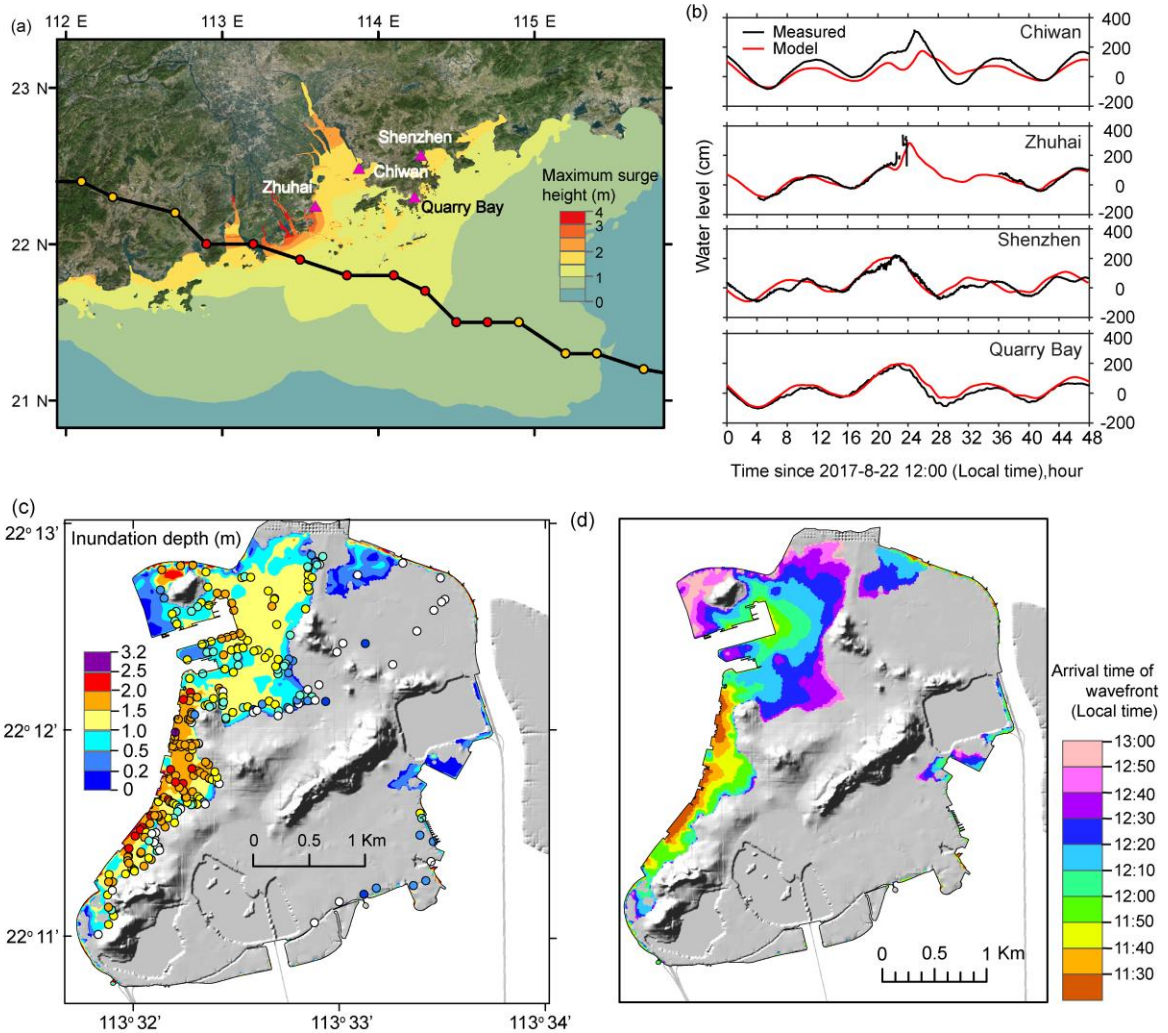

433

434 **Figure 6.** Numerical results capture well the key features of storm flooding induced by Typhoon Hato. (a) The
435 simulated maximum surge height in the PRE; (b) A comparison of simulated and measured storm tide at four
436 selected tide locations (marked with the green dots in Figure 5a). Note the measured data at Zhuhai station is not
437 complete due to a power cut; (c) The surveyed inundation depths (the colored dots) overlaid on the simulated
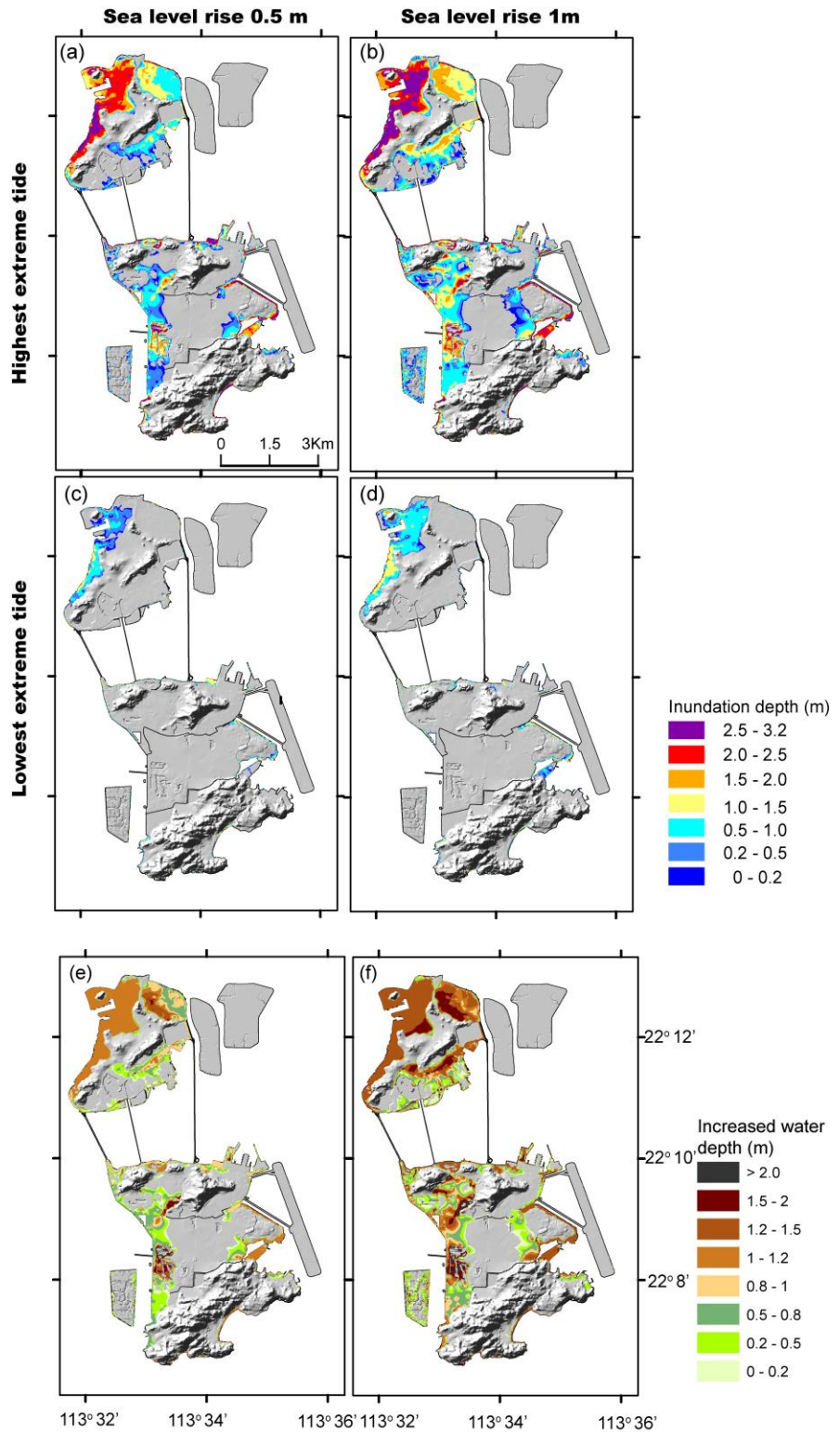438 maximum inundation depths in the Macau Peninsula; (d) The arrival time of the flood wavefront.

439
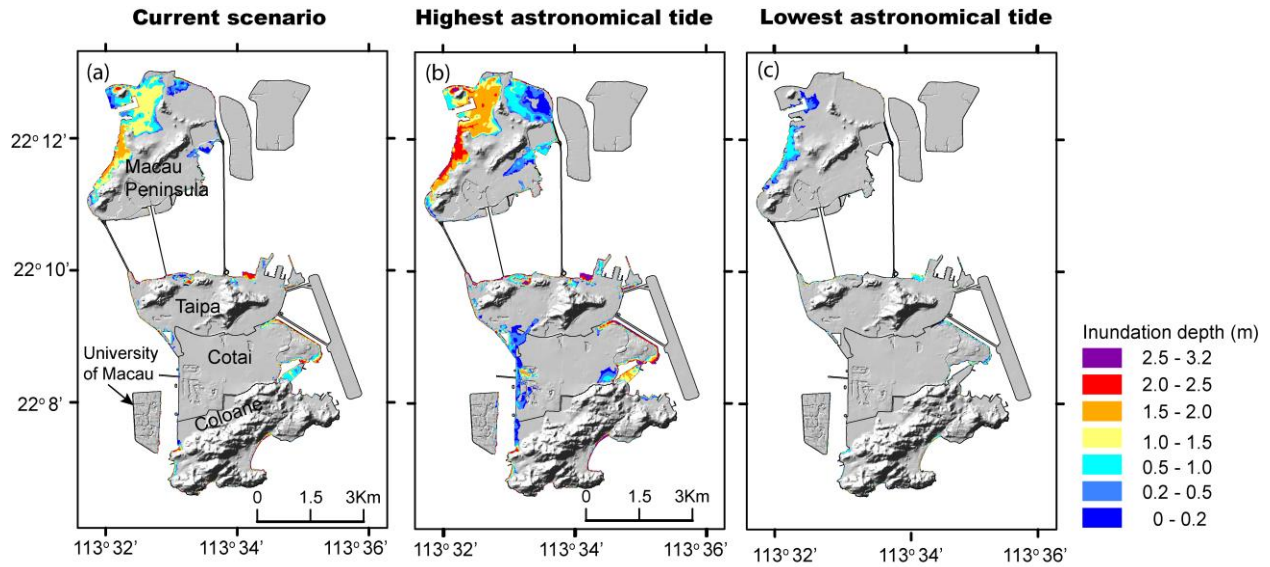
Figure 7. Maximum inundation depths for (a) the benchmark scenario; (b) the highest extreme tide and (c) the lowest extreme tide under the current sea level.

442
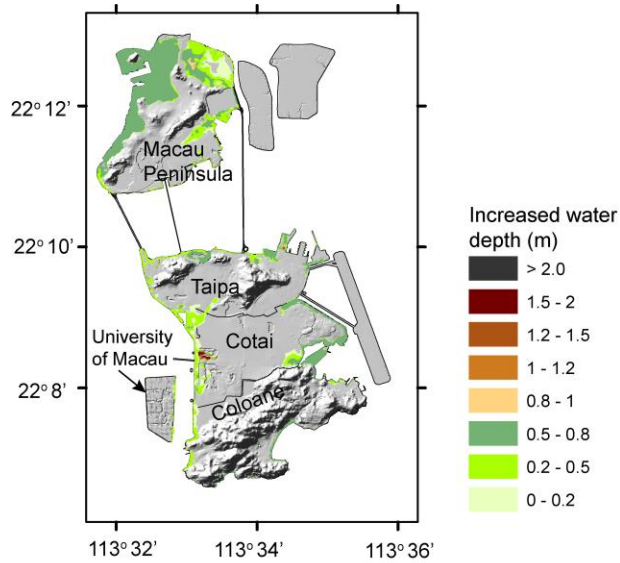
Figure 8. A map showing the difference between the maximum inundation during the benchmark scenario (Figure 5a) and the highest extreme tide under the current sea level.
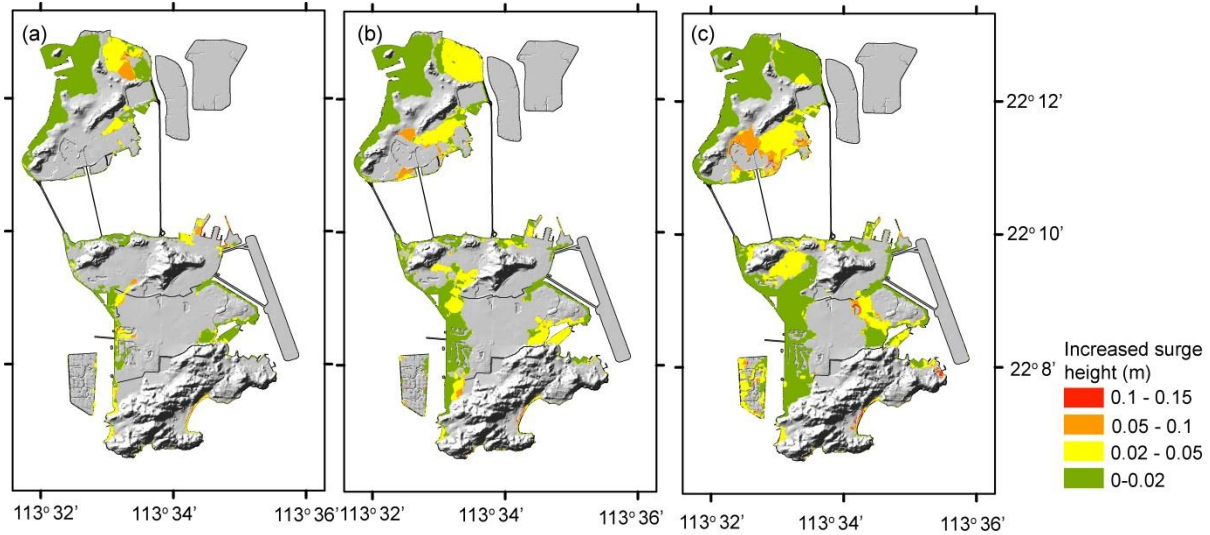
19

Figure 9. Maximum inundation depths during the highest extreme tide under (a) 0.5-m SLR and (b) 1-m SLR. Maximum inundation depth during the lowest extreme tide under (c) 0.5-m SLR and (d) 1-m SLR; A map showing

449   the difference between the maximum inundation during the benchmark scenario (Figure 7a) and the highest

450   extreme tide under (e) 0.5-m SLR and (f) 1-m SLR.

451

452

453   **Figure 10.** The difference in maximum inundation depths between scenarios with and without the wave model

454   during the highest extreme tide under (a) the current sea level (b) 0.5-m SLR, and (c) 1-m SLR.